1    **Scaling estimates of vegetation structure in Amazonian tropical forests using**

2    **multi-angle MODIS observations**

3

4    Yhasmin Mendes de Moura[1*]

5    Thomas Hilker[2, 3]

6    Fabio Guimarães Goncalves[4]

7    Lênio Soares Galvão[1]

8    João Roberto dos Santos[1]

9    Alexei Lyapustin[5]

10   Eduardo Eiji Maeda[6]

11   Camila Valéria de Jesus Silva[1]

12

13   [1]Instituto Nacional de Pesquisas Espaciais (INPE), Divisão de Sensoriamento Remoto,

14   12245-970, São José dos Campos, SP, Brazil.

15   [2]Oregon State University, College of Forestry, Corvallis, OR, 97331, USA.

16   [3]University of Southampton, Department of Geography and Environment,

17   Southampton, SO17 1BJ, United Kingdom

18   [4]Agrosatelite Geotecnologia Aplicada, Florianópolis, SC, 88032-005, Brazil.

19   [5]NASA Goddard Space Flight Center, Greenbelt, MD, 20771, USA.

20   [6]University of Helsinki, Department of Geosciences and Geography, P.O. Box 68, FI-

21   00014, Helsinki, Finland

22

23   *Corresponding author: yhas.mendes@gmail.com

24    **Abstract.** Detailed knowledge of vegetation structure is required for accurate modelling

25    of terrestrial ecosystems, but direct measurements of the three dimensional distribution

26    of canopy elements, for instance from LiDAR, are not widely available. We investigate

27    the potential for modelling vegetation roughness, a key parameter for climatological

28    models, from directional scattering of visible and near-infrared (NIR) reflectance

29    acquired from NASA's Moderate Resolution Imaging Spectroradiometer (MODIS). We

30    compare our estimates across different tropical forest types to independent measures

31    obtained from: (1) airborne laser scanning (ALS), (2) spaceborne Geoscience Laser

32    Altimeter System (GLAS)/ICESat, and (3) the spaceborne SeaWinds/QSCAT. Our

33    results showed linear correlation between MODIS-derived anisotropy to ALS-derived

34    entropy ($r^2$= 0.54, RMSE=0.11), even in high biomass regions. Significant relationships

35    were also obtained between MODIS-derived anisotropy and GLAS-derived entropy

36    ($0.52 \leq r^2 \leq 0.61$; $p<0.05$), with similar slopes and offsets found throughout the season,

37    and RMSE between 0.26 and 0.30 (units of entropy). The relationships between the

38    MODIS-derived    anisotropy    and    backscattering    measurements    ($\sigma^0$)    from

39    SeaWinds/QuikSCAT presented an $r^2$ of 0.59 and a RMSE of 0.11. We conclude that

40    multi-angular MODIS observations are suitable to extrapolate measures of canopy

41    entropy across different forest types, providing additional estimates of vegetation

42    structure in the Amazon.

43

44    *Keywords:* canopy roughness, multi-angle, MODIS, MAIAC, LiDAR, anisotropy

45

46

**1. Introduction**

Terrestrial vegetation plays a significant role in the re-distribution of moisture and heat in the surface boundary layer, as well as in the energy balance of the planet (Bastiaanssen et al., 1998a). Land-atmosphere interactions are driven by the three-dimensional structure of vegetated land cover, including surface roughness, leaf area and canopy volume (Vourlitis et al., 2015; Domingues et al., 2005). Canopy roughness, defined as vertical irregularities in the height of the canopy (Chapin et al., 2011), plays a key role in earth system modelling. For instance, evapotranspiration is controlled much more by canopy roughness (and therefore aerodynamic conductance) than by canopy leaf area or maximum stomatal conductance (Chapin et al., 2011).

At stand level scales, significant advances have been made measuring canopy vegetation structure from Light Detection and Ranging (LiDAR). LiDAR allows direct measurements of the three-dimensional distribution of vertical vegetation elements from ground-based (Strahler et al., 2008), airborne (Wulder et al., 2012) and orbital platforms (Sun et al., 2008). To date, most vegetation related LiDAR applications rely on airborne platforms for data acquisition, with measurements acquired at altitudes between 500 and 3000 m (Hilker et al., 2010). Due to cost and practical considerations, the availability of airborne LiDAR is currently limited to specific research sites and data are not available across the landscape.

The Geoscience Laser Altimeter System (GLAS), onboard the Ice, Cloud, and land Elevation Satellite (ICESat), has provided certain capability to map vegetation characteristics across broader areas from space (Zwally et al., 2002). GLAS is a large-footprint, waveform-recording LiDAR that measures the timing and power of the 1064 nm laser energy returned from illuminated surfaces (Schutz et al., 2005). While not configured for vegetation characterization, the GLAS instrument allows quantification

of the vertical distribution of plant components relative to the ground over vegetated terrain (Harding, 2005; Yu et al., 2015, Morton et al., 2014). GLAS data has been successfully used to discriminate forest structure across various biome types (Boudreau et al., 2008; Gonçalves, 2014; Lefsky et al., 2005; Pang et al., 2008) and to estimate canopy light environments and forest productivity (Stark et al., 2014; Rap et al., 2015; Morton et al., 2016). While GLAS provides larger spatial coverage, its footprint is still spatially discrete and importantly a lack of repeated measurements prevents its use for estimation of climate related responses of vegetation.

Perhaps complimentary to structural observations, optical remote sensing available from satellite data, provide global coverage at frequent time steps but can generally not deliver accurate information on the vertical organization of plant canopies. For instance, vegetation indices provide general information on canopy "greenness" but their ability to detect changes in high-biomass areas is limited due to a well-documented saturation effect (Carlson and Ripley, 1997). Although VIs have been employed as proxies for vegetation structure, including roughness lengths for turbulent transfer, field estimates of vegetation structure attributes are often only moderately correlated with VIs and their derivatives (Glenn et al., 2008).

As an alternative to conventional, mono-angle observations, the combination of multiple view angles may provide new opportunities for modelling the structure of vegetated land surfaces (Breunig et al., 2015; Shaw & Pereira, 1982) from optical remote sensing. Changes in canopy structure including changes in tree crown size, shape, density and spatial distribution of leaves, affect the directional scattering of light (Chen et al., 2005). Multi-angle observations of this scattering may therefore allow us to describe the three-dimensional structure of vegetation (Chen and Leblanc, 1997; Strahler & Jupp, 1990). Multi-angular scattering of surface reflectance (anisotropy) has

98  been linked to optical properties and geometric structure of the target (Widlowski et al.,

99  2004; Widlowski et al., 2005), including canopy roughness (Strahler, 2009), leaf angle

100 distribution (Roujean, 2002), leaf area index (LAI) (Walthall, 1997) and foliage

101 clumping (Chen et al., 2005; Chopping et al., 2011). Such estimates may even be made

102 in dense canopies (Moura et al., 2015), as observations acquired from multiple view

103 angles decrease the dispersion and saturation effect in geometrically complex vegetation

104 (Zhang et al., 2002).

105

106     With the advent of multi-angular sensors such as the Multi-angle Imaging

107 SpectroRadiometer (MISR) (Breunig et al., 2015) and POLDER (Roujean, 2002), the

108 dependence of reflectance on observation angles has been documented (Barnsley et al.,

109 2004) and modelled (Roujean et al., 1992; Wanner et al., 1995). Recent progress using

110 the Multi-Angle Implementation of Atmospheric Correction Algorithm (MAIAC) has

111 allowed the acquisition of multi-angle reflectance across large areas and at high

112 observation frequencies by combining satellite imagery obtained from NASA's

113 Moderate Resolution Imaging Spectroradiometer (MODIS) Terra and Aqua platforms

114 during a few overpasses (Lyapustin et al., 2012a; Moura et al., 2015). Such observations

115 could potentially allow periodic and spatially contiguous estimates of vegetation

116 structure and its response to changes in climate variables. When correlated with more

117 direct measurements of canopy structure by other instruments, such as LiDAR, this may

118 then allow us to extrapolate canopy roughness and other structural estimates in space

119 and time, thereby filling key data gaps for improving our understanding of ecosystem

120 structure and functioning. Further validation may be provided by scatterometer

121 observations over dense forests. For instance, the SeaWinds microwave radar, onboard

122 NASA's QuikSCAT satellite, was primarily designed to measure near-surface wind

123 speed and direction over the oceans. However, due to its high sensitivity to water

124    content that drives canopy dielectric properties, it has been also used to study canopy

125    structure (Frolking et al., 2011; Saatchi et al., 2013).

126    In this study, we used estimates of canopy roughness obtained from 1) airborne

127    laser scanning (ALS), 2) spaceborne LiDAR GLAS, and 3) the spaceborne SeaWinds

128    scatterometer, to evaluate the potential of multi-angular MODIS observations for

129    modelling vegetation roughness from directional scattering of visible and near-infrared

130    (NIR) reflectance. We implemented a spatial scaling approach, from airborne to orbital

131    levels of data acquisition, to model continuous coverage of roughness across tropical

132    forests of the Xingu basin area in the Brazilian Amazon. Our objective was to test

133    whether multi-angle MODIS reflectance can be used as a proxy for canopy roughness

134    over Amazonian tropical forests, including different forest types such as Dense and

135    Open ombrophilous Forests, and Semi-Deciduous Forest.

136

137    **2. Methods**

138    *2.1. Study area*

139    The study area is located in the southeast part of the Amazon, including the Xingu

140    basin and adjacent areas (Figure 1). Figure 1 also shows the GLAS transects for the

141    study area (Schutz et al., 2005) as well as the ALS and the field data plots. The study

142    area presents a south-north gradient with respect to climate. Following the Köppen

143    classification, the southern portion of the study area is dominated by tropical wet and

144    dry climate (Aw), while the north portion is characterized by tropical monsoon climate

145    (Am). Length and duration of the dry season, defined as months with rainfall less than

146    100 mm or less than one third of precipitation range (Asner & Alencar, 2010; Myneni et

147    al., 2007), also varies across the study area. In the southern parts, the dry season lasts

148    about five months, from May to September (Moura et al., 2012). In the northern parts, a

149    drier climate prevails between July and November (Vieira et al., 2004). The area is

150    characterized by three predominant forest types: Dense Ombrophilous Forest (Dse),

151    Open Ombrophilous Forest (Asc) and Semi-Deciduous Forest (Fse) (IBGE, 2004).

152

153                                            **(Figure 1)**

154

155    *2.2. Field inventory data*

156        Estimates of vegetation structure were derived for each of the three different forest

157    types using available inventory plots across the region. For two vegetation types, Open

158    Ombrophilous Forest (Asc) and Semi-decidiuous Forest (Fse), surveys were provided

159    by the Sustainable Landscapes Brazil project in collaboration with the Brazilian

160    Agricultural Research Corporation (EMBRAPA), the US Forest Service, the USAID,

161    and the US Department of State (http://mapas.cnpm.embrapa.br/paisagenssustentaveis/).

162    The Asc forest type was represented by 22 plots of 40 m x 40 m each. All the trees with

163    a diameter at breast height (DBH) equal to or greater than 10 cm were measured within

164    each plot. For Fse, 10 sample plots (20 m x 500 m) were used. The field data for the

165    Dense Ombrophilous Forest (Dse) were obtained in 2012 and are described in Silva et

166    al. (2015). The floristic and structural surveys included seven sample plots of 25 m x

167    100 m over mature forests. Trees with DBH equal to or greater than 10 cm were

168    measured within each plot.

169

170    *2.3. Airborne Laser Scanning (ALS) data*

171        ALS data were acquired by GEOID Ltd. using an Altm 3100/Optech instrument

172    and provided by the Sustainable Landscapes Brazil project. The positional accuracy (1σ)

173    of the LiDAR measurements was approximately 0.10 m horizontally and 0.12 m

174 vertically (http://mapas.cnpm.embrapa.br/paisagenssustentaveis/). We focussed our

175 analysis on undisturbed, non-degraded research plots. Structural information was

176 obtained in the Tapajós National Forest, Pará State (September to November 2012), in

177 São Félix do Xingu municipality, Pará state (August 2012) and in Canarana/Querência

178 municipality, Mato Grosso State (August 2012), to represent Dse, Asc and Fse,

179 respectively. Table 1 shows the specifications of LiDAR data for each site.

180 **(Table 1)**

181 ALS data were delivered as classified LAS-formatted point clouds, along with 1-m

182 resolution bare earth digital terrain models (DTM). For comparison with GLAS,

183 discrete-return data were aggregated produce pseudo-waveforms. Coops et al. (2007)

184 demonstrated that canopy profiles, analogue to those derived from full waveform

185 systems, can be derived from discrete return LiDAR when aggregating returns into three

186 dimensional voxel spaces and comparing the amount of discrete returns contained in

187 each voxel layer to the voxel layers below and above. In this study, waveforms were

188 synthesized by sub-setting the LiDAR point cloud co-located with each field plot and

189 counting the number of points observed in vertical bins of 50 cm and at a horizontal

190 resolution of 100 x100m. 10 by 10 pixels of LiDAR metrics were then averaged to

191 match the 1x1km MODIS pixel size. ALS based entropy was then computed to

192 determine canopy structural diversity and approximate canopy roughness (Palace et al.,

193 2015; Stark et al., 2012). The method is described in detail in the next section (2.4) and

194 is analogue to that applied from GLAS observations. In addition to ALS entropy, we

195 also calculated canopy volume models (CVMs) to quantify the three-dimensional

196 structure of the forest canopies based on the incident radiation levels and

197 photosynthetic potential (Coops et al., 2007; Hilker et al., 2010). The method is

198  described in detail in (Lefsky et al., 2005). CVMs divide the canopy space into sunlit and

199  shaded vegetation elements as well as gap spaces enclosed within.

200

201  ### 2.4. GLAS/ICESat data and structural metrics from vertical profiles

202  GLAS profiles were obtained across the Xingu basin (Figure 1) between 2006 and

203  2008 (laser operating periods 3E through 2D) (Gonçalves, 2014). Each GLAS footprint

204  is elliptical in shape, spaced at approximately 170-m intervals along-track. GLAS

205  LiDAR profiles characteristics varied between the campaigns across the study area. The

206  near-infrared elliptical footprint and eccentricity varied between 51.2 (±1.7) to 58.7

207  (±0.6), and 0.48 (±0.02) to 0.59 (±0.01), respectively. The horizontal and vertical

208  geolocation accuracy varied between 0.00 (±3.41) to 1.72 (±7.36), and 0.00 (±2.38) to

209  1.2 (±5.14), depending on the campaign and respective data product.

210  Because GLAS observations are able to penetrate optically thin clouds (Schulz et

211  al., 2005), processing of the GLAS profiles included additional cloud screening to

212  improve the data quality. The technique is described in detail in Smith et al. (2005).

213  Briefly, the approach takes advantage of the fact that returns unaffected by saturation or

214  forward scattering resemble narrow Gaussian pulses that are similar to the transmitted

215  pulse (Smith et al., 2005). To process GLAS waveforms, we used parameters reported

216  in the GLA01, GLA05, and GLA14 data products following methods described by

217  (Gonçalves, 2014). First, the waveforms were filtered by convolution with a discrete

218  Gaussian kernel with the same standard deviation as the transmitted laser pulse. This

219  procedure reduced the background noise, while preserving an adequate level of detail

220  for characterization of the canopy (Sun et al., 2008). Second, GLAS waveforms used in

221  this study were calibrated and digitized into 1000 discrete bins at a time resolution of 1

222  ns (~15 cm). The locations of the highest (signal start) and lowest (signal end) detected

223    surfaces within the 150-m waveform were determined, respectively, as the first and last

224    elevations at which the amplitude exceeded a threshold level, for a minimum of $n$

225    consecutive bins. The peak of the ground return was determined as the lowest peaks in

226    the smoothed waveforms with at least the same width as the transmitted laser pulse,

227    after taking into account the mean noise level. In order to minimize the effect of

228    different output energy levels of the 2E and 3E Laser flight campaigns, all profiles were

229    then normalized to unity by dividing by the maximum amplitude. This correction

230    approach assumes that differences in measurement campaigns affect the overall amount

231    of energy but do not significantly change the waveforms (i.e. the vertical scale of energy

232    output) of our entropy calculation (Gonçalves, 2014).

233        We utilized GLAS estimates of entropy ($S_z$), a measure of canopy structural

234    diversity sensitive to crown depth and leaf area (Palace et al., 2015; Stark et al., 2012),

235    as a proxy of canopy roughness. $S_z$ was calculated using Equations 1 and 2 (Harding &

236    Carabajal, 2005, Nelson et al., 2009, Treuhaft et al., 2009, Gonçalves, 2014):

237

238    
$$S_z = -\sum_{i=1}^{n_b} p(w_i)\,\ln(p(w_i)),\ \ with$$

239                                                       (1)

240    
$$p(w_i) = \frac{w_i(z)}{\int_0^{H100} w_i(z)\,dz}$$

241                                                       (2)

242    where $n_b$ is the number of vertical bins from the ground peak to the signal start defined

243    as the vertical distance between the ground peak and the signal start; w(z) is the laser

244    power received from the 1m bin centered at height z; H100 is the maximum canopy

245    height, defined as the vertical distance between the ground peak and the signal start

246    (Gonçalves, 2014).

247

248    *2.5. SeaWinds/QuikSCAT data*

249    Estimates of canopy structure were independently also obtained from SeaWinds

250    Scatterometer data, provided by NASA's Scatterometer Climate Record Pathfinder

251    project. The SeaWinds Scatterometer operates at microwave frequency of 13.4 GHz

252    (Ku-band) with mean incidence angle of 54º for V-polarization and 46º for H-

253    polarization. The sensitivity of radar data to variations in vegetation canopy structure

254    can be explained by the dependence of radar backscatter to surface dielectric properties,

255    which are strongly dependent on the liquid water content of the canopy constituents

256    (Frolking et al., 2006). Given that the SeaWinds instrument operates at a higher

257    frequency and higher incidence angle than other similar sensors, it has lower penetration

258    into forest canopy, and therefore almost no interference from soil moisture variations in

259    densely vegetated forested areas (Saatchi et al., 2013).

260    The backscatter product ($\sigma^0$) used in this study combines ascending (morning) and

261    descending (evening) orbital passes, and is based on SeaWinds "egg" images (Frolking

262    et al., 2006). The nominal image pixel resolution for egg images is 4.45 km/pixel. Only

263    backscatter data for horizontal (H) polarization were used, as previous assessments had

264    indicated that results using vertical (V) polarization show no significant differences

265    (Saatchi et al., 2013). We used data obtained from January 2001 to November 2009,

266    when the sensor stopped collecting data due to failure in the scanning capability. To

267    match the spatial resolution of the SeaWinds instrument, we averaged the corresponding

268    anisotropy    observations    from    the    MODIS    instrument    to    match    the

269    SeaWinds/QuikSCAT pixels.

270 *2.6. Determination of surface anisotropy from multi-angle MODIS data*

271    MODIS observations are acquired at different solar and view zenith angles,

272 depending on the orbital overpass and time of the year. Pixel-based algorithms often

273 assume a Lambertian reflectance model, which reduces the anisotropy of the derived

274 surface reflectance (Lyapustin, 1999; Wang et al., 2010), thus decreasing the ability to

275 detect directional scattering (Hilker et al., 2009). In this study, we use the MAIAC

276 algorithm because it preserves the multi-angle character of MODIS observations,

277 providing a means to estimate the anisotropy of surface reflectance (Chen et al., 2005),

278 a surrogate for structure of vegetation and shaded parts of the canopy (Myneni et al.,

279 2002; Chen et al., 2003; Gao et al., 2003). MAIAC is a cloud screening and atmospheric

280 correction algorithm that uses an adaptive time series analysis and processing of groups

281 of pixels to derive atmospheric aerosol concentration and surface reflectance. A detailed

282 description of the technique can be found in Lyapustin et al. (2011) and Lyapustin et al.

283 (2012). Previous results (Hilker et al., 2012, 2015) have shown that while the MAIAC

284 cloud mask is less conservative, it is also more accurate, improving the number of

285 observations and data quality in tropical environments.

286    For retrieval of the surface bi-directional reflectance distribution function (BRDF),

287 MAIAC accumulates data over 4-16 days (Lyapustin et al., 2011, 2012). Assuming that

288 vegetation is relatively stable during this period, the surface directional scattering can be

289 characterized using the Ross-Thick Li-Sparse (RTLS) bidirectional reflectance

290 distribution function (BRDF) model (Roujean, et al., 1992).

291    Using the RTLS model (Wanner et al., 1995), we characterized the BRDF of each 1

292 km x 1 km grid cell of MODIS data. Based on the RTLS BRDF model, we derived

293 MODIS backscatter (Solar Zenith Angle (SZA) = 45°, View Zenith Angle (VZA) = 35°,

294 Relative Azimuth Angle (RAA) = 180°) and forward scatter (SZA = 45°, VZA = 35°,

295    RAA = 0°) observations (4-16 days of observations) for a fixed view and sun angle. The

296    advantage of using the RTLS model rather than reflectance directly is to keep constant

297    sun-observer geometry and extrapolate measurements to the principal plane. In addition,

298    the modelled reflectance can be based on all multi-angle MODIS data, which should

299    yield a more representative characterization of the reflectance properties. We selected a

300    VZA of 35° rather than the hotspot location at VZA = 45° in order to keep the modelled

301    reflectance closer to the actual range of angles observed by MODIS, thereby

302    minimizing potential errors resulting from extrapolation of the BRDF.

303    We used estimates of anisotropy (defined as the difference between BRDF

304    modelled backscattering (SZA = 45°, VZA = 35°, RAA = 180°) and BRDF modelled

305    forward scattering (SZA = 45°, VZA = 35°, RAA = 0°) based on the Enhanced

306    Vegetation Index (EVI) to describe roughness of the surface for different vegetation

307    types across the study area (Moura et al., 2015). The objective of using EVI rather than

308    surface reflectance of a given band was to minimize the effect of non-photosynthetically

309    active elements (i.e. soil fraction component) while optimizing the sensitivity to green

310    canopy structure (Moura et al., 2015).

311    MODIS-derived anisotropy values were then regressed against ALS-derived

312    entropy, GLAS-derived entropy and SeaWinds/QuikSCAT backscatter ($\sigma^0$, Frolking et

313    al., 2006), which were estimated on a per-pixel-basis to generate time series profiles of

314    entropy for each forest type in the study area.

315

316    **3. Results**

317    The Xingu basin contains a number of different forest types. However, vegetation is

318    dominated by Asc and Dse forest types in the north, and by Fse vegetation in the south,

319   as illustrated in Figure 2. The GLAS tracks are also shown in this figure to highlight the

320   sampling density of the spaceborne LiDAR over each forest type. An illustration of the

321   mean canopy height (MCH) derived from ALS for three sample areas of 1 ha each is

322   provided in Figure 2. Airborne ALS measurements showed, on average, the largest tree

323   heights in the Dse class with values up to 40 meters tall (red color in the inset of Figure

324   2). Asc and Fse vegetation types reached up to 30 m and 25 meters in height,

325   respectively. Field measurements showed that mean canopy heights from forest

326   inventories were 19.8 m, 17.4 m and 17.0 m for Dse, Asc and Fse, respectively (Table

327   2). When compared to Asc and Fse, Dse presented larger metrics of diversity (i.e.

328   species richness (S) and Shannon index (H')) and structure (mean height ($H_T$), mean

329   diameter at breast height (DBH), basal area (BA), aboveground biomass (AGB) and leaf

330   area index (LAI)) (Table 2).

331

332                                    **(Figure 2)**

333

334                                    **(Table 2)**

335   Differences in canopy structure were also evident from the analysis of canopy

336   volume models (CVMs) (Figure 3). While gap spaces were relatively small in all three

337   vegetation types, Asc showed a notably higher proportion of sunlit vegetation that

338   reached down deep into the canopy, suggesting a higher spatial variability of tree

339   heights compared to the other two vegetation types. Similarly, gaps in the upper canopy

340   were mostly present in Asc, as expected for open forest types. Fse showed gaps

341   predominantly in lower height levels, and a higher overall proportion of shaded crown.

342   Full canopy closure (100% of the canopy space filled by either sunlit or shaded canopy

343 elements or fully enclosed gap space) was reached at about 15 m height for both Asc

344 and Dse, and at about 20 m height for Fse.

345 **(Figure 3)**

346

347 Differences in vegetation structure derived from ALS data were confirmed also

348 with spaceborne GLAS observations. GLAS-derived seasonal profiles of entropy for

349 2006 showed spatial averages that differed over time between the three vegetation types

350 (Figure 4). Even though there were differences in the years of data acquisition (2006 for

351 GLAS and 2012 for ALS), the shaded area in Figure 4 was plotted to provide a seasonal

352 reference between the airborne and spaceborne data. GLAS derived seasonal profiles

353 varied between different forest types. The lowest values of entropy were consistently

354 found for Fse. In contrast, Asc for Dse showed GLAS entropy higher throughout the

355 measurement period. All forest types showed strong seasonality with increasing entropy

356 from February to September, and decreasing values thereafter with predominance of

357 higher entropy during the dry season.

358

359 **(Figure 4)**

360 Examples of MODIS anisotropy during March, June and October of 2006

361 illustrated seasonal and spatial changes in multi-angle reflectance across the Xingu

362 basin (Figure 5). The MODIS derived anisotropy was consistently higher in the northern

363 part of the study area, and its spatial distribution coincided well with the forest types

364 indicated in Figure 2. A clear limit between forested (high MODIS anisotropy) and non-

365 forested (low anisotropy) areas was evident in the southern part of the map.

366 Furthermore, higher values of anisotropy were found for the Asc and Dse vegetation

367 compared to Fse. While MAIAC observations allowed a notable number of

368     measurements of anisotropy between June (Figure 5b) and October (Figure 5c), some

369     data gaps were observed in March (Figure 5a) due to cloud cover in the rainy season.

370     **(Figure 5)**

371     MODIS-derived anisotropy was linearly correlated to ALS-derived entropy

372     (Figure 6). The coefficient of determination ($r^2$) of the relationship between all 828

373     MODIS pixels that coincided with existing ALS observations was 0.54 with an RMSE

374     of 0.11 units of entropy. Much of the scattering presented in Figure 3 was limited to

375     lower values of entropy, while residuals were notably smaller for the higher entropy

376     range.

377     **(Figure 6)**

378     Significant relationships were also found between MODIS anisotropy and

379     GLAS measured entropy using all observations that contained five or more GLAS shots

380     within the 1 km x 1 km MODIS pixels (Figure 7). In order to examine seasonal

381     variability in the relationship, we performed the regressions separately for March

382     (Figure 7a), June (Figure 7b) and October (Figure 7c) of 2006. The $r^2$ varied between

383     0.52 for March and 0.61 for June (p<0.05) with similar slopes and offsets found

384     throughout the observation period. RMSE varied between 0.26 and 0.30 units of entropy.

385     The highest noise levels were observed in March, which is corresponding also to the

386     larger amount of data gaps during the rainy season (Figure 5). The availability of GLAS

387     data was somewhat limited during June, but the relationships were still highly

388     significant and consistent with those observed during other months of the year. A

389     comparison between conventional VI estimates using directionally normalized EVI

390     from MAIAC and LiDAR derived Entropy is shown in the appendix (Figure A1).

391     **(Figure 7)**

392    A strong relationship between the MODIS-derived anisotropy and the

393    backscattering measurements ($\sigma^0$) from SeaWinds/QuikSCAT was also observed

394    (Figure 8). The relationship was obtained for 10.000 randomly sampled MODIS pixels

395    and corresponding SeaWinds/QuikSCAT ($\sigma^0$) observations across the Xingu basin for

396    all available QuikSCAT data between 2001 and 2009. Note, however, that when using

397    radar observations, the relationship to MODIS-derived anisotropy was non-linear

398    ($r^2$=0.59, RMSE=0.11).

399    **(Figure 8)**

400    Time series profiles of MODIS-derived entropy estimated from the regression

401    model of Figure 7c and of MODIS-derived QuikSCAT-$\sigma^0$ estimated from model of

402    Figure 8 were plotted as spatial averages for Dse, Asc and Fse (Figure 9). All three

403    forest types displayed notable seasonal cycles. The Ombrophilous Forests (Dse and Asc)

404    consistently showed high values of entropy with less seasonal variation. In contrast, the

405    seasonal cycles were much more pronouced in the Fse, as expected for semi-decidous

406    vegetation. Both models (GLAS-derived entropy and QScat-derived $\sigma^0$) yielded very

407    similar seasonal patterns, in terms of temporal variation as well as in terms of

408    differences between vegetation types. The results presented in Figure 9 were consistent

409    also with those shown in Figure 5. A small negative trend in both entropy and $\sigma^0$ was

410    observed from 2000 until 2009 and a positive trend in all three vegetation types was

411    found from 2010 onwards. This trend was especially pronounced for the canopy entropy

412    based on GLAS observations.

413    **(Figure 9)**

414    **4. Discussion**

415    This study investigated the potential of multi-angle reflectance obtained from

416    MODIS to derive estimates of vegetated surface roughness as an important structural

417   parameter of land atmosphere interactions. Aside from field observations, airborne laser

418   scanning is arguably the most comprehensive tool to describe the three-dimensional

419   vegetation structure at the stand level to date (Coops et al., 2007; Lim et al., 2003;

420   Wulder et al., 2012). Recent initiatives such as the "Sustainable Landscapes

421   Brazil" project (http://mapas.cnpm.embrapa.br/paisagenssustentaveis/) seek to improve

422   upon existing deficiencies of data availability and provide new opportunities to generate

423   structural metrics across discrete locations within the Amazon basin.

424   LiDAR based characterization of vegetation structure (Figures 2, 3, and Table 1)

425   exposed a large heterogeneity across the Xingu basin, both spatially and seasonally.

426   ALS-observed structural differences between vegetation types were detectable also

427   from space using photon counting LiDAR (GLAS/IceSat) and microwave

428   backscattering (SeaWinds/QuikSCAT) (Figures 4 and 9b). This is an important finding,

429   as it opens an opportunity for scaling spatially discrete observations of canopy structure

430   across larger areas from space (Popescu et al., 2011).

431   Spatial and temporal heterogeneity in Amazonian vegetation (Silva et al., 2013;

432   Townsend et al., 2008) is not easily obtained from conventional vegetation indices

433   (Hilker et al., 2015), as VIs cannot adequately capture differences in canopy structure

434   among different vegetation types (Glenn et al., 2008; Lagouarde et al., 2002). Findings

435   presented in this study (Figures 6 to 9) suggest that such canopy structural variation may

436   be better determined from multi-angular reflectance. Our estimates of anisotropy

437   showed considerable improvements over estimates using mono-observation vegetation

438   indices (Figure A1). The ability of multi-angle observation to derive vegetation

439   structural attributes is well supported by previous results (Chen & Leblanc, 1997; Chen,

440   2003; Gao, 2003; Strahler & Jupp, 1990; Yu et al., 2015; Zhang et al., 2002). While

441   these authors have focused on smaller study areas using specialized sensors, our

442    findings confirm such multi-angle potential to be acquired from the MODIS instrument

443    and across the Amazon basin (Moura et al., 2015). Our previous work also confirmed

444    the consistency of monthly anisotropy measurements and its statistical significance for

445    estimating seasonal changes in vegetation structure across the Amazon (Moura et al.,

446    2015). This is an important advancement, as it allows structural estimates over large

447    areas and at high temporal frequencies from space, complementing the data analysis of

448    orbital LiDAR data.

449    Anisotropy derived from multiple overpasses of MODIS imagery may therefore

450    provide new insights into structural variability of Amazon forests as it increases the

451    sensitivity to changes in vegetation structure across dense vegetation types. As

452    demonstrated in previous work (Moura et al., 2015), seasonal changes in observed

453    anisotropy cannot be explained by bi-directional effects, as all observations have been

454    normalized to a fixed forward and backscatter geometry (Lyapustin et al., 2012b). In

455    addition, Moura et al. (2015) demonstrated that standard deviations between observed

456    and modelled MAIAC reflectance were about 10% of the observed variation in

457    anisotropy, thus confirming the ability of our approach to detect seasonal and inter-

458    annual changes. Differences between forward and backscatter observations as utilized in

459    this paper are largely driven by the different directional scattering behaviour of red and

460    NIR reflectance (Moura et al., 2015, Hilker et al., 2015). The modelled near hotspot and

461    near darkspot locations were designed to maximize the range of resulting anisotropy,

462    thereby seeking to increase the sensitivity with respect to changes in vegetation

463    structure.

464    While the range of view angles acquired by MODIS is relatively small, as the

465    instrument was not specifically designed for multi-angle acquisitions, MODIS-derived

466    anisotropy still provided an effective means to characterize vegetation structure across

467 large areas from space. Within the Amazon basin (or tropics in general), this is partially

468 facilitated by the fact that MODIS view geometry comes very close to the principal

469 plane twice a year. As a result, our BRDF model is representative of the angles used in

470 this study. Consequently, modelled anisotropy is close to its maximum range of possible

471 values. The contrary occurs in mid-latitudes where observations are further from the

472 principal plane. In these cases, other geometric configurations might be preferable.

473     Modelling MODIS anisotropy using the RTLS BRDF model further allowed us to

474 derive anisotropy independent of the sun-observer geometry (Roujean et al., 1992). As a

475 limitation to this approach, changes in sun-sensor configuration over the year do not

476 always allow modelling of forward and backscattering observations within the sampling

477 range of the MODIS instruments. Therefore, higher uncertainties may be observed

478 during some times of the year than during others.

479     The strong, positive correlation found between GLAS-measured entropy and

480 MODIS anisotropy (Figure 6) may be explained by geometric scattering of individual

481 tree crowns (Chopping et al., 2011; Li, X., Strahler, 1986). For instance, a large

482 variability in canopy heights (high canopy roughness) will increase the geometric

483 scattering component, especially of NIR reflectance. Other structural changes may,

484 however, also influence seasonal patterns of anisotropy. In addition to canopy

485 roughness, anisotropy is also affected by leaf angle distribution (Roujean, 2002) and

486 foliage clumping (Chen et al., 2005) among other variables related to the floristic

487 variability, which tends to be high in tropical forests. The interaction between these

488 variables and multi-angle scattering is not straightforward, requiring further

489 investigation, especially in the components of scattering determined in the RTLS model.

490 For example, increases in leaf area may increase the volumetric scattering component

491 (Ross, 1981; Roujean, et al., 1992) of multi-angle reflectance, but at the same time

492    decrease the surface roughness, at least within a certain range of values. Therefore, the

493    results presented in here should be understood as a first demonstration of the technique.

494         Due to the complexities described as well as other limitations in terms of footprint

495    size, and range of angular sampling, MODIS-derived estimates of canopy structure

496    should not be understood as a replacement for direct 3D measures of vegetation, but

497    rather as a complimentary approach for scaling such observations in space and time.

498    The consistency in the modelled relationship obtained from GLAS LiDAR and

499    SeaWinds/QuikSCAT backscattering is encouraging in this respect, as it suggests that

500    such scaling approaches may be built on opportunistically sampled observations across

501    platforms. For instance, MODIS data can help interpret estimates of canopy roughness

502    in between GLAS footprints, as well as fill missing observations in time, enabling more

503    comprehensive seasonal and spatial analysis. Upcoming new LiDAR instruments, such

504    as the Global Ecosystem Dynamics (GEDI) mission (Dubayah et al., 2014; Stysley et al.,

505    2015), will allow further improvements in the measures of canopy structure as well as

506    biomass.

507

508    **5. Conclusions**

509         Our analysis has demonstrated that multi-angular MODIS observations are suitable

510    to determine canopy entropy at different scales of LiDAR measurements across the

511    study area in the Amazon. The sparseness of existing, highly detailed LiDAR

512    observations currently imposes severe restriction on accuracy of modeled carbon and

513    water fluxes, particularly in remote regions such as the Amazon basin. Complementary

514    measures of vegetation structure from optical satellites are therefore highly desirable to

515    extrapolate spatially or temporally sparse estimates of canopy structure across the

516 landscape. Such approaches will be crucial for improving our understanding of climate

517 tolerance and responses to Amazonian forests to extreme events.

518

530

531 **References**

532 Asner, G. P., & Alencar, A. (2010). Drought impacts on the Amazon forest: the remote
533      sensing perspective. *The New Phytologist*, *187*(3), 569–78. doi:10.1111/j.1469-
534      8137.2010.03310.x

535 Barnsley, M. J., Settle, J. J., Cutter, M. A., Lobb, D. R., & Teston, F. (2004). The
536      PROBA/CHRIS mission: a low-cost smallsat for hyperspectral multiangle
537      observations of the Earth surface and atmosphere. *IEEE Transactions on
538      Geoscience and Remote Sensing*, *42*(7), 1512–1520.
539      doi:10.1109/TGRS.2004.827260

540 BOUDREAU, J., NELSON, R., MARGOLIS, H., BEAUDOIN, A., GUINDON, L., &
541      KIMES, D. (2008). Regional aboveground forest biomass using airborne and
542      spaceborne LiDAR in Québec. *Remote Sensing of Environment*, *112*(10), 3876–
543      3890. doi:10.1016/j.rse.2008.06.003

544 Breunig, F. M., Galvão, L. S., dos Santos, J. R., Gitelson, A. A., de Moura, Y. M., Teles,
545      T. S., & Gaida, W. (2015). Spectral anisotropy of subtropical deciduous forest
546      using MISR and MODIS data acquired under large seasonal variation in solar
547      zenith angle. *International Journal of Applied Earth Observation and*

548    *Geoinformation*, *35*, 294–304. doi:10.1016/j.jag.2014.09.017

549    Carlson, T. N., & Ripley, D. A. (1997). On the relation between NDVI, fractional
550    vegetation cover, and leaf area index. *Remote Sensing of Environment*, *62*(3), 241–
551    252. doi:10.1016/S0034-4257(97)00104-1

552    Chapin, F. I., Matson, P., & Vitousek, P. (2011). *Principles of terrestrial ecosystem*
553    *ecology*. Retrieved from
554    https://books.google.com/books?hl=en&lr=&id=68nFNpceRmIC&oi=fnd&pg=PR
555    5&dq=principles+of+terrestrial+ecosystem+ecology+stuart&ots=V1DZdx8sni&si
556    g=d5RF0D75OjOWRvQpqdU9k1hxqkI

557    Chen, J. M., & Leblanc, S. G. (1997). A four-scale bidirectional reflectance model
558    based on canopy architecture. *IEEE Transactions on Geoscience and Remote*
559    *Sensing*, *35*(5), 1316–1337. doi:10.1109/36.628798

560    Chen, J. M., Liub, J., Leblanc, S. G., Lacazec, R., & Roujean, J. L. (2003). Multi-
561    angular optical remote sensing for assessing vegetation structure and carbon
562    absorption.

563    Chen, J. M., Menges, C. H., & Leblanc, S. G. (2005). Global mapping of foliage
564    clumping index using multi-angular satellite data. *Remote Sensing of Environment*,
565    *97*(4), 447–457. doi:10.1016/j.rse.2005.05.003

566    Chopping, M., Schaaf, C. B., Zhao, F., Wang, Z., Nolin, A. W., Moisen, G. G.,
567    Martonchik, J. V., & Bull, M. (2011). Forest structure and aboveground biomass in
568    the southwestern United States from MODIS and MISR. *Remote Sensing of*
569    *Environment*, *115*(11), 2943–2953. doi:10.1016/j.rse.2010.08.031

570    Coops, N. C., Hilker, T., Wulder, M. A., St-Onge, B., Newnham, G., Siggins, A., &
571    Trofymow, J. A. (Tony). (2007). Estimating canopy structure of Douglas-fir forest
572    stands from discrete-return LiDAR. *Trees*, *21*(3), 295–310. doi:10.1007/s00468-
573    006-0119-6

574    Domingues, T. F., Berry, J. A., Martinelli, L. A., Ometto, J. P. H. B., & Ehleringer, J. R.
575    (2005). Parameterization of Canopy Structure and Leaf-Level Gas Exchange for an
576    Eastern Amazonian Tropical Rain Forest (Tapajós National Forest, Pará, Brazil).
577    *Earth Interactions*, *9*(17), 1–23. doi:10.1175/EI149.1

578    Dubayah, R., Goetz, S. J., Blair, J. B., Fatoyinbo, T. E., Hansen, M., Healey, S. P.,
579    Hofton, M. A., Hurtt, G. C., Kellner, J., Luthcke, S. B., & Swatantran, A.
580    (2014). The Global Ecosystem Dynamics Investigation. *American Geophysical*
581    *Union*. Retrieved from http://adsabs.harvard.edu/abs/2014AGUFM.U14A..07D

582    Frolking, S., Milliman, T., McDonald, K., Kimball, J., Zhao, M., & Fahnestock, M.
583    (2006). Evaluation of the Sea Winds scatterometer for regional monitoring of
584    vegetation phenology. *Journal of Geophysical Research: Atmospheres*, *111*(17), 1–
585    14. doi:10.1029/2005JD006588

586    Frolking, S., Milliman, T., Palace, M., Wisser, D., Lammers, R., & Fahnestock, M.
587    (2011). Tropical forest backscatter anomaly evident in SeaWinds scatterometer
588    morning overpass data during 2005 drought in Amazonia. *Remote Sensing of*
589    *Environment*, *115*(3), 897–907. doi:10.1016/j.rse.2010.11.017

590    Gao, F. (2003). Detecting vegetation structure using a kernel-based BRDF model.
591    *Remote Sensing of Environment*, *86*(2), 198–205. doi:10.1016/S0034-
592    4257(03)00100-7

593    Glenn, E. P., Huete, A. R., Nagler, P. L., & Nelson, S. G. (2008). Relationship between

594      remotely-sensed vegetation indices, canopy attributes and plant physiological
595      processes: What vegetation indices can and cannot tell us about the landscape.
596      *Sensors*, *8*(4), 2136–2160. doi:10.3390/s8042136

597    Gonçalves, F. G. (2016, January). Vertical structure and aboveground biomass of
598      tropical forests from lidar remote sensing.

599    Harding, D. J. (2005). ICESat waveform measurements of within-footprint topographic
600      relief and vegetation vertical structure. *Geophysical Research Letters*, *32*(21),
601      L21S10. doi:10.1029/2005GL023471

602    Hilker, T., Leeuwen, M., Coops, N. C., Wulder, M. A., Newnham, G. J., Jupp, D. L. B.,
603      & Culvenor, D. S. (2010). Comparing canopy metrics derived from terrestrial and
604      airborne laser scanning in a Douglas-fir dominated forest stand. *Trees*, *24*(5), 819–
605      832. doi:10.1007/s00468-010-0452-7

606    Hilker, T., Lyapustin, A. I., Hall, F. G., Myneni, R., Knyazikhin, Y., Wang, Y., Tucker,
607      C. J., & Sellers, P. J. (2015). On the measurability of change in Amazon vegetation
608      from MODIS. *Remote Sensing of Environment*, *166*, 233–242.
609      doi:10.1016/j.rse.2015.05.020

610    Hilker, T., Wulder, M. A., Coops, N. C., Linke, J., McDermid, G., Masek, J. G., Gao, F.,
611      & White, J. C. (2009). A new data fusion model for high spatial- and temporal-
612      resolution mapping of forest disturbance based on Landsat and MODIS. *Remote
613      Sensing of Environment*, *113*(8), 1613–1627. doi:10.1016/j.rse.2009.03.007

614    IBGE. (2004). *Manual Tecnico da vegetacao brasileira*.

615    Jing M. Chena, Jane Liub, Sylvain G. Leblancb, Roselyne Lacazec, J.-L. R. (2002).
616      Multi-angular optical remote sensing for assessing vegetation structure and carbon
617      absorption. *Remote Sensing of Environment*, *84*, 516–525.

618    Lagouarde, J.-P., Jacob, F., Gu, X. F., Olioso, A., Bonnefond, J.-M., Kerr, Y., John
619      Mcaneney, K., & Irvine, M. (2002). Spatialization of sensible heat flux over a
620      heterogeneous landscape. *Agronomie*, *22*(6), 627–633. doi:10.1051/agro:2002032

621    Lefsky, M. A., Harding, D. J., Keller, M., Cohen, W. B., Carabajal, C. C., Del Bom
622      Espirito-Santo, F., Hunter, M. O., & de Oliveira, R. (2005). Estimates of forest
623      canopy height and aboveground biomass using ICESat. *Geophysical Research
624      Letters*, *32*(22), L22S02. doi:10.1029/2005GL023971

625    Li, X., Strahler, A. H. (1986). Geometric-Optical Bidirectional Reflectance Modeling of
626      a Conifer Forest Canopy, (6), 906–919.

627    Lim, K., Treitz, P., Wulder, M., St-Onge, B., & Flood, M. (2003). LiDAR remote
628      sensing of forest structure. *Progress in Physical Geography*, *27*(1), 88–106.
629      doi:10.1191/0309133303pp360ra

630    LYAPUSTIN, A. I., & MULDASHEV, T. Z. (1999). METHOD OF SPHERICAL
631      HARMONICS IN THE RADIATIVE TRANSFER PROBLEM WITH NON-
632      LAMBERTIAN SURFACE. *Journal of Quantitative Spectroscopy and Radiative
633      Transfer*, *61*(4), 545–555. doi:10.1016/S0022-4073(98)00041-7

634    Lyapustin, A. I., Wang, Y., Laszlo, I., Hilker, T., G.Hall, F., Sellers, P. J., Tucker, C. J.,
635      & Korkin, S. V. (2012a). Multi-Angle Implementation of Atmospheric Correction
636      for MODIS (MAIAC). Part 3: Atmospheric Correction. *Remote Sensing of
637      Environment*, *127*, 385–393. doi:10.1016/j.rse.2012.09.002

638    Lyapustin, A., Wang, Y., Laszlo, I., & Hilker, T. (2012b). Multi-Angle Implementation

of Atmospheric Correction for MODIS (MAIAC). Part 3: Atmospheric Correction. *Remote Sensing of Environment*, *127*, 385–393. Retrieved from http://ntrs.nasa.gov/search.jsp?R=20120017006

Moura, Y. M. de, Hilker, T., Lyapustin, A. I., Galvão, L. S., dos Santos, J. R., Anderson, L. O., de Sousa, C. H. R., & Arai, E. (2015). Seasonality and drought effects of Amazonian forests observed from multi-angle satellite data. *Remote Sensing of Environment*, *171*, 278–290. doi:10.1016/j.rse.2015.10.015

Moura, Y. M., Galvão, L. S., dos Santos, J. R., Roberts, D. a., & Breunig, F. M. (2012). Use of MISR/Terra data to study intra- and inter-annual EVI variations in the dry season of tropical forest. *Remote Sensing of Environment*, *127*, 260–270. doi:10.1016/j.rse.2012.09.013

Myneni, R. ., Hoffman, S., Knyazikhin, Y., Privette, J. ., Glassy, J., Tian, Y., Wang, Y., Song, X., Zhang, Y., Smith, G. ., Lotsch, A., Friedl, M., Morisette, J. ., Votava, P., Nemani, R. ., & Running, S. . (2002). Global products of vegetation leaf area and fraction absorbed PAR from year one of MODIS data. *Remote Sensing of Environment*, *83*(1-2), 214–231. doi:10.1016/S0034-4257(02)00074-3

Myneni, R. B., Yang, W., Nemani, R. R., Huete, A. R., Dickinson, R. E., Knyazikhin, Y., Didan, K., Fu, R., Negrón Juárez, R. I., Saatchi, S. S., Hashimoto, H., Ichii, K., Shabanov, N. V, Tan, B., Ratana, P., Privette, J. L., Morisette, J. T., … Salomonson, V. V. (2007). Large seasonal swings in leaf area of Amazon rainforests. *Proceedings of the National Academy of Sciences of the United States of America*, *104*(12), 4820–3. doi:10.1073/pnas.0611338104

Palace, M. W., Sullivan, F. B., Ducey, M. J., Treuhaft, R. N., Herrick, C., Shimbo, J. Z., & Mota-E-Silva, J. (2015). Estimating forest structure in a tropical forest using field measurements, a synthetic model and discrete return lidar data. *Remote Sensing of Environment*, *161*, 1–11. doi:10.1016/j.rse.2015.01.020

Pang, Y., Lefsky, M., Sun, G., Miller, M. E., & Li, Z. (2008). Temperate forest height estimation performance using ICESat GLAS data from different observation periods, *37*.

Popescu, S. C., Zhao, K., Neuenschwander, A., & Lin, C. (2011). Satellite lidar vs. small footprint airborne lidar: Comparing the accuracy of aboveground biomass estimates and forest structure metrics at footprint level. *Remote Sensing of Environment*, *115*(11), 2786–2797. doi:10.1016/j.rse.2011.01.026

Ross, I. (1981). *The radiation regime and architecture of plant stands*.

Roujean, J. J.-L., Leroy, M., & Deschamps, P.-Y. (1992). A bidirectional reflectance model of the Earth's surface for the correction of remote sensing data. *Journal of Geophysical Research*, *97*(D18), 20455–20468. doi:10.1029/92JD01411

Roujean, J.-L. (2002). Global mapping of vegetation parameters from POLDER multiangular measurements for studies of surface-atmosphere interactions: A pragmatic method and its validation. *Journal of Geophysical Research*, *107*(D12), 4150. doi:10.1029/2001JD000751

Saatchi, S., Asefi-Najafabady, S., Malhi, Y., Aragão, L. E. O. C., Anderson, L. O., Myneni, R. B., & Nemani, R. (2013). Persistent effects of a severe drought on Amazonian forest canopy. *Proceedings of the National Academy of Sciences of the United States of America*, *110*(2), 565–70. doi:10.1073/pnas.1204651110

Schutz, B. E., Zwally, H. J., Shuman, C. A., Hancock, D., & DiMarzio, J. P. (2005).

685    Overview of the ICESat Mission. *Geophysical Research Letters*, *32*(21), L21S01.
686        doi:10.1029/2005GL024009

687    Shaw, R. H., & Pereira, A. . (1982). Aerodynamic roughness of a plant canopy: A
688        numerical experiment. *Agricultural Meteorology*, *26*(1), 51–65. doi:10.1016/0002-
689        1571(82)90057-7

690    Silva, F. B., Shimabukuro, Y. E., Aragão, L. E. O. C., Anderson, L. O., Pereira, G.,
691        Cardozo, F., & Arai, E. (2013). Large-scale heterogeneity of Amazonian
692        phenology revealed from 26-year long AVHRR/NDVI time-series. *Environmental*
693        *Research Letters*, *8*(2), 024011. doi:10.1088/1748-9326/8/2/024011

694    Stark, S. C., Leitold, V., Wu, J. L., Hunter, M. O., de Castilho, C. V, Costa, F. R. C.,
695        McMahon, S. M., Parker, G. G., Shimabukuro, M. T., Lefsky, M. A., Keller, M.,
696        Alves, L. F., Schietti, J., Shimabukuro, Y. E., Brandão, D. O., Woodcock, T. K.,
697        Higuchi, N., … Chave, J. (2012). Amazon forest carbon dynamics predicted by
698        profiles of canopy leaf area and light environment. *Ecology Letters*, *15*(12), 1406–
699        14. doi:10.1111/j.1461-0248.2012.01864.x

700    Strahler, A. H. (2009). Vegetation canopy reflectance modeling—recent developments
701        and remote sensing perspectives* . *Remote Sensing Reviews*, *15*(1-4), 179–194.
702        doi:10.1080/02757259709532337

703    Strahler, A. H., Jupp, D. L. ., Woodcock, C. E., Schaaf, C. B., Yao, T., Zhao, F., Yang,
704        X., Lovell, J., Culvenor, D., Newnham, G., Ni-Miester, W., & Boykin-Morris, W.
705        (2008). Retrieval of forest structural parameters using a ground-based lidar
706        instrument (Echidna ® ). *Canadian Journal of Remote Sensing*, *34*(S2), S426–
707        S440. doi:10.5589/m08-046

708    Strahler, A. H., & Jupp, D. L. B. (1990). Modeling bidirectional reflectance of forests
709        and woodlands using boolean models and geometric optics. *Remote Sensing of*
710        *Environment*, *34*(3), 153–166. doi:10.1016/0034-4257(90)90065-T

711    Stysley, P. R., Coyle, D. B., Kay, R. B., Frederickson, R., Poulios, D., Cory, K., &
712        Clarke, G. (2015). Long term performance of the High Output Maximum
713        Efficiency Resonator (HOMER) laser for NASA′s Global Ecosystem Dynamics
714        Investigation (GEDI) lidar. *Optics & Laser Technology*, *68*, 67–72.
715        doi:10.1016/j.optlastec.2014.11.001

716    SUN, G., RANSON, K., KIMES, D., BLAIR, J., & KOVACS, K. (2008). Forest
717        vertical structure from GLAS: An evaluation using LVIS and SRTM data. *Remote*
718        *Sensing of Environment*, *112*(1), 107–117. doi:10.1016/j.rse.2006.09.036

719    Townsend, A. R., Asner, G. P., & Cleveland, C. C. (2008). The biogeochemical
720        heterogeneity of tropical forests. *Trends in Ecology & Evolution*, *23*(8), 424–31.
721        doi:10.1016/j.tree.2008.04.009

722    Vieira, S., de Camargo, P. B., Selhorst, D., da Silva, R., Hutyra, L., Chambers, J. Q.,
723        Brown, I. F., Higuchi, N., dos Santos, J., Wofsy, S. C., Trumbore, S. E., &
724        Martinelli, L. A. (2004). Forest structure and carbon dynamics in Amazonian
725        tropical rain forests. *Oecologia*, *140*(3), 468–79. doi:10.1007/s00442-004-1598-z

726    Vourlitis, G. L., de Souza Nogueira, J., de Almeida Lobo, F., & Pinto, O. B. (2015).
727        Variations in evapotranspiration and climate for an Amazonian semi-deciduous
728        forest over seasonal, annual, and El Niño cycles. *International Journal of*
729        *Biometeorology*, *59*(2), 217–30. doi:10.1007/s00484-014-0837-1

730    Walthall, C. L. (1997). A Study of Reflectance Anisotropy and Canopy Structure Using

731     a Simple Empirical Model. *Remote Sensing of Environment*, *128*(May 1995), 118–
732     128.

733 Wang, Y., Lyapustin, A. I. A., Privette, J. J. L., Cook, R. B., SanthanaVannan, S. K.,
734     Vermote, E. F., & Schaaf, C. L. (2010). Assessment of biases in MODIS surface
735     reflectance due to Lambertian approximation. *Remote Sensing of …*, *114*(11),
736     2791–2801. doi:10.1016/j.rse.2010.06.013

737 Wanner, W., Li, X., & Strahler, A. H. (1995). On the derivation of kernels for kernel-
738     driven models of bidirectional reflectance. *Journal of Geophysical Research*,
739     *100*(D10), 21077. doi:10.1029/95JD02371

740 WIDLOWSKI, J.-L., PINTY, B., GOBRON, N., Verstraete, M. M., Diner, D. J., &
741     Davis, A. B. (2004). Canopy Structure Parameters Derived from Multi-Angular
742     Remote Sensing Data for Terrestrial Carbon Studies. *Climatic Change*, *67*(2-3),
743     403–415. doi:10.1007/s10584-004-3566-3

744 Widlowski, J.-L., Pinty, B., Lavergne, T., Verstraete, M. M., & Gobron, N. (2005).
745     Using 1-D models to interpret the reflectance anisotropy of 3-D canopy targets:
746     issues and caveats. *IEEE Transactions on Geoscience and Remote Sensing*, *43*(9),
747     2008–2017. doi:10.1109/TGRS.2005.853718

748 Wulder, M. a., White, J. C., Nelson, R. F., Næsset, E., Ørka, H. O., Coops, N. C., Hilker,
749     T., Bater, C. W., & Gobakken, T. (2012). Lidar sampling for large-area forest
750     characterization: A review. *Remote Sensing of Environment*, *121*, 196–209.
751     doi:10.1016/j.rse.2012.02.001

752 Yu, Y., Yang, X., & Fan, W. (2015). Estimates of forest structure parameters from
753     GLAS data and multi-angle imaging spectrometer data. *International Journal of
754     Applied Earth Observation and Geoinformation*, *38*, 65–71.
755     doi:10.1016/j.jag.2014.12.013

756 Zhang, Y., Tian, Y., Myneni, R. B., Knyazikhin, Y., & Woodcock, C. E. (2002).
757     Assessing the information content of multiangle satellite data for mapping biomes.
758     *Remote Sensing of Environment*, *80*(3), 418–434. Retrieved from
759     http://www.sciencedirect.com/science/article/pii/S0034425701003224

760 Zwally, H. J., Schutz, B., Abdalati, W., Abshire, J., Bentley, C., Brenner, A., Bufton, J.,
761     Dezio, J., Hancock, D., Harding, D., Herring, T., Minster, B., Quinn, K., Palm, S.,
762     Spinhirne, J., & Thomas, R. (2002). ICESat's laser measurements of polar ice,
763     atmosphere, ocean, and land. *Journal of Geodynamics*, *34*(3-4), 405–445.
764     doi:10.1016/S0264-3707(02)00042-X

765

766

767

768

769

770

**LIST OF TABLES**

Table 1. Characteristics of the airborne laser scanning (ALS) data acquired over Dense Ombrophilous (Dse), Open Ombrophilous (Asc) and Semi-Deciduous (Fse) Forests in the Brazilian Amazon.

| Forest Type | Total area (ha) | Max flight altitude (m) | Flightline overlap (%) | Average return density (ppm$^2$) | Average first return density (ppm$^2$) | Field of view (°) |
|---|---|---|---|---|---|---|
| Dse | 1049 | 850 | 65 | 25.1 | 15.28 | 11.1 |
| Asc | 1004 | 850 | 65 | 24.1 | 15.20 | 11.0 |
| Fse | 1005 | 850 | 65 | 13.7 | 7.05 | 11.0 |

Table 2. Floristic and structural metrics calculated from field inventory data for Dense Ombrophilous Forest (Dse), Open Ombrophilous Forest (Asc) and Semi-Deciduous Forest (Fse). The mean leaf area index (LAI), determined from Airborne Laser Scanning (ALS), is indicated in the last column of the table.

| Forest Type | Plots | S | H' | Ht$_{(m)}$ | BA$_{(m^2 m^{-2})}$ | LAI $_{(ALS)}$ |
|---|---|---|---|---|---|---|
| Dse | 7 | 181 | 4.61 | 18.1 | 30.63 | 6.05 |
| Asc | 22 | 1595 | 3.67 | 17.4 | 11.36 | 4.32 |
| Fse | 10 | 802 | 2.20 | 17.0 | 12.83 | 5.33 |

788 **LIST OF FIGURES**

789

790 Figure 1. Location of the study within the Amazon basin. The inset shows the

791 Geoscience Laser Altimeter System (GLAS) coverage (strings), airborne laser scanning

792 (ALS) data acquisition and the available field inventory plots across the Xingu basin.

793 Figure 2. Vegetation cover map adapted from IBGE (2004) in the left, and diagrams of

794 height estimates from ALS LiDAR data in the right, to illustrate structural variation

795 between the three predominant forest types in the study area (Dse, Asc and Fse). Each

796 Airborne Laser Scanning (ALS) plot represents an area of 100 m x100 m to describe the

797 heights in the three different forests.

798 Figure 3. Canopy volume models (CVMs) based on the Airborne Laser Scanning (ALS)

799 for (a) Dense ombrophilous forest (Dse); (b) Open ombrophilous Forest (Asc); and (c)

800 Semi-deciduous forest (Fse).

801 Figure 4. Seasonal profiles of GLAS-derived entropy for the three different forest types

802 of the study area. GLAS data were obtained only for the months indicated in the x-axis.

803 Just for reference, the shaded area represents the quarter when the Airborne Laser

804 Scanning (ALS) data were collected in 2012.

805 Figure 5. MODIS-derived anisotropy images during (a) March, (b) June and (c) October

806 of 2006 to illustrate seasonal and spatial changes in multi-angle reflectance across the
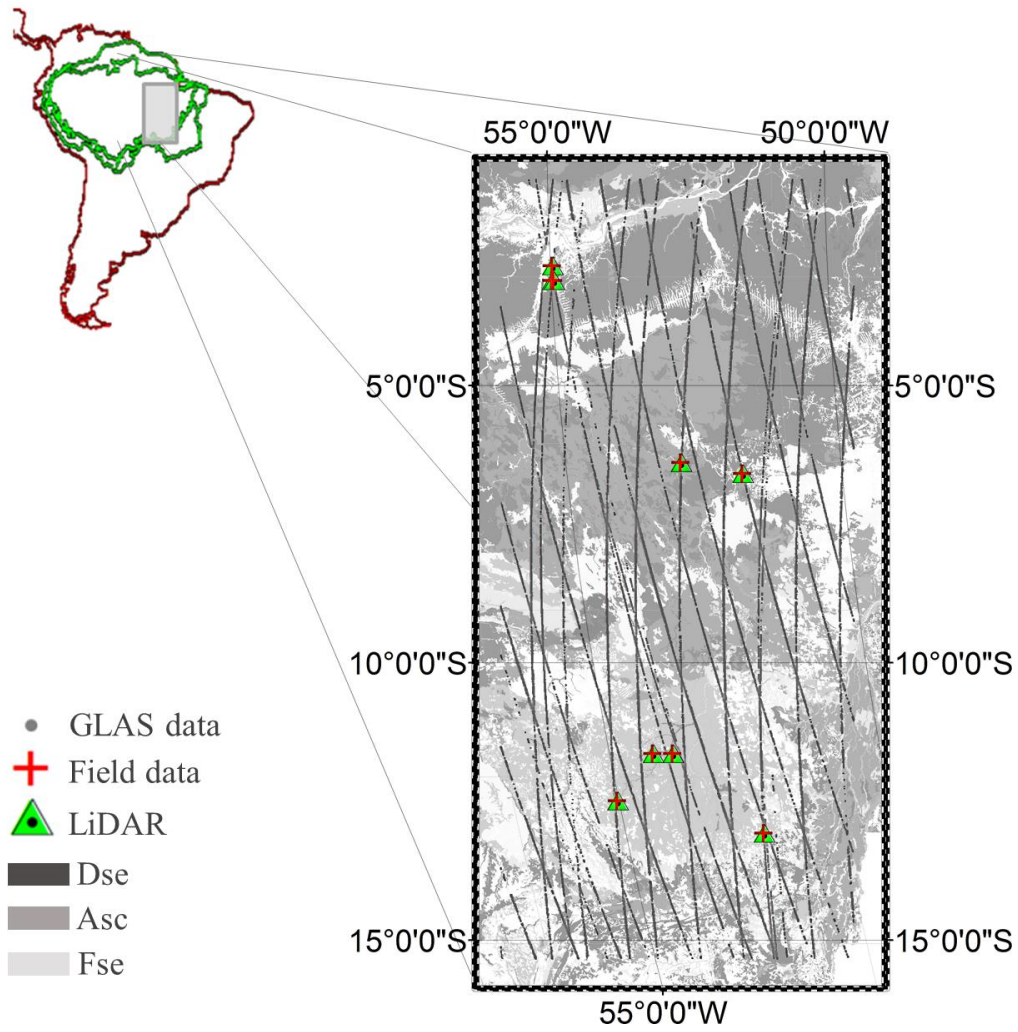
807 Xingu basin.

808 Figure 6. Relationship between MODIS-derived anisotropy and ALS-derived entropy

809 (or canopy roughness).

810 Figure 7. Relationship between MODIS-derived anisotropy and GLAS-derived entropy

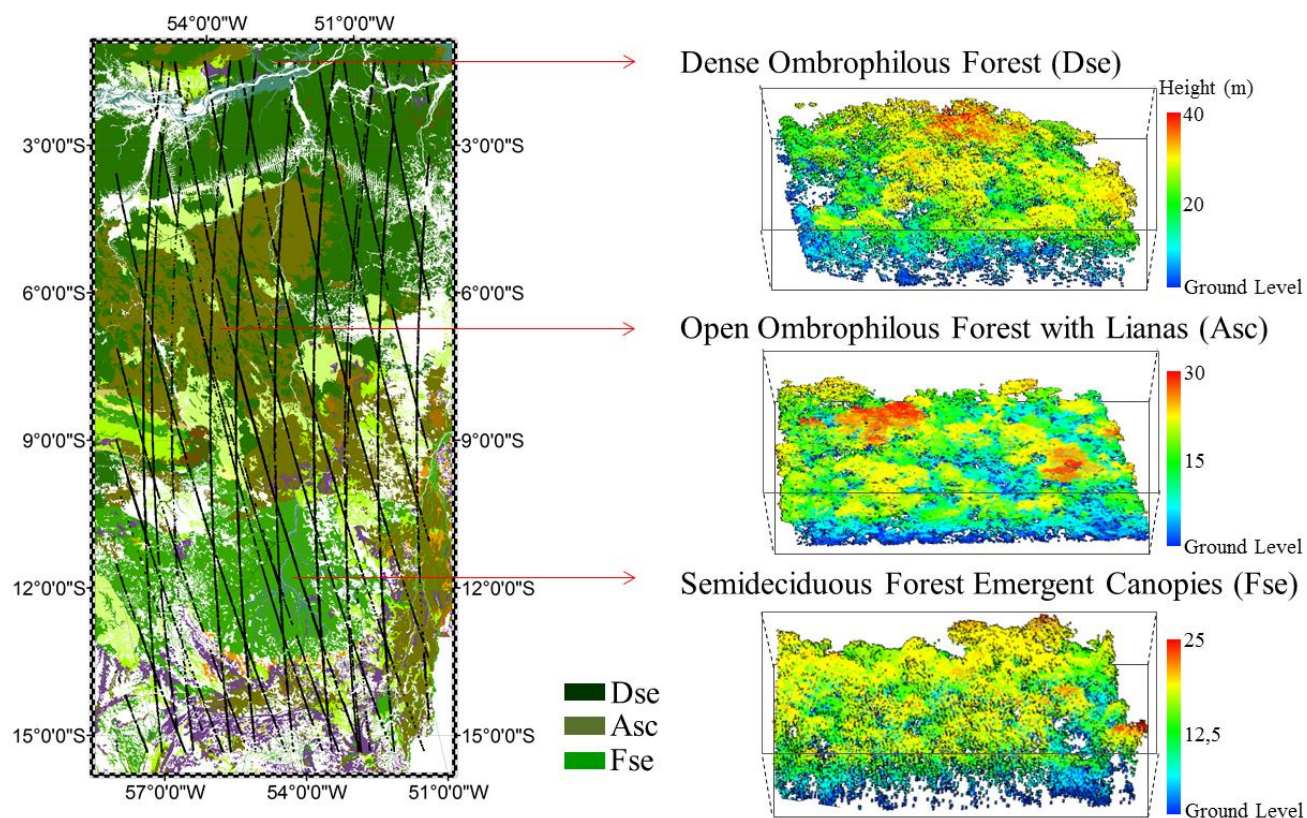811 using observations for (a) March, (b) June and (c) October of 2006.

812 Figure 8. Relationship between MODIS-derived anisotropy and backscattering ($\sigma^0$)

813 measurements from SeaWinds/QSCAT over Amazonian tropical forests considering the

814 period 2001 to 2009.

815 Figure 9. Time series profiles of MODIS-derived (a) GLAS entropy estimated using the

816 regression model of Figure 7c, and (b) MODIS-derived SeaWinds/QuikSCAT

817 backscattering ($\sigma^0$) from the model of Figure 8. Results are shown as spatial average for

818 Dense (Dse) and Open (Asc) Ombrophilous Forests and the Semi-Deciduous Forest

819 (Fse) between 2000 and 2012 for the Xingu basin.

820

821 Figure A1. Comparison between MODIS-MAIAC EVI (normalized for directional

822 effects) and estimates of canopy entropy derived from ALS (a), GLAS (b) and

823 QuikSCAT (c). The vegetation index was significantly less suited to describe canopy
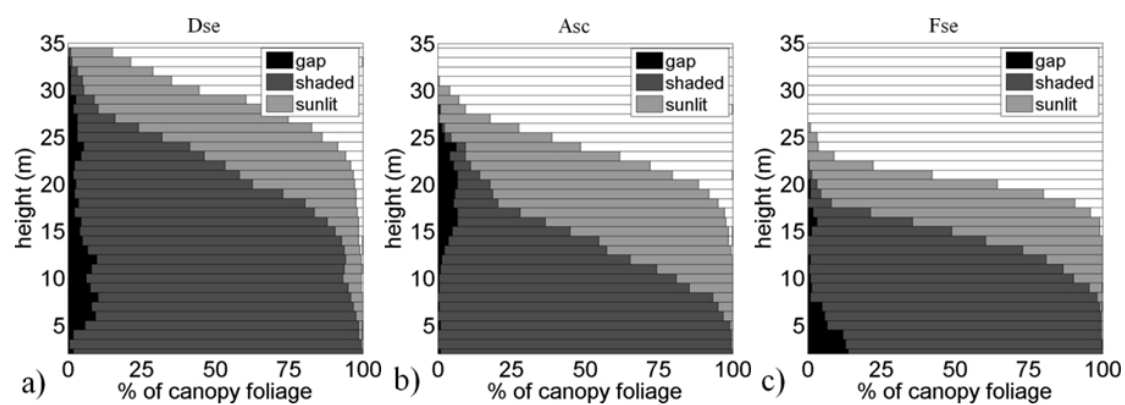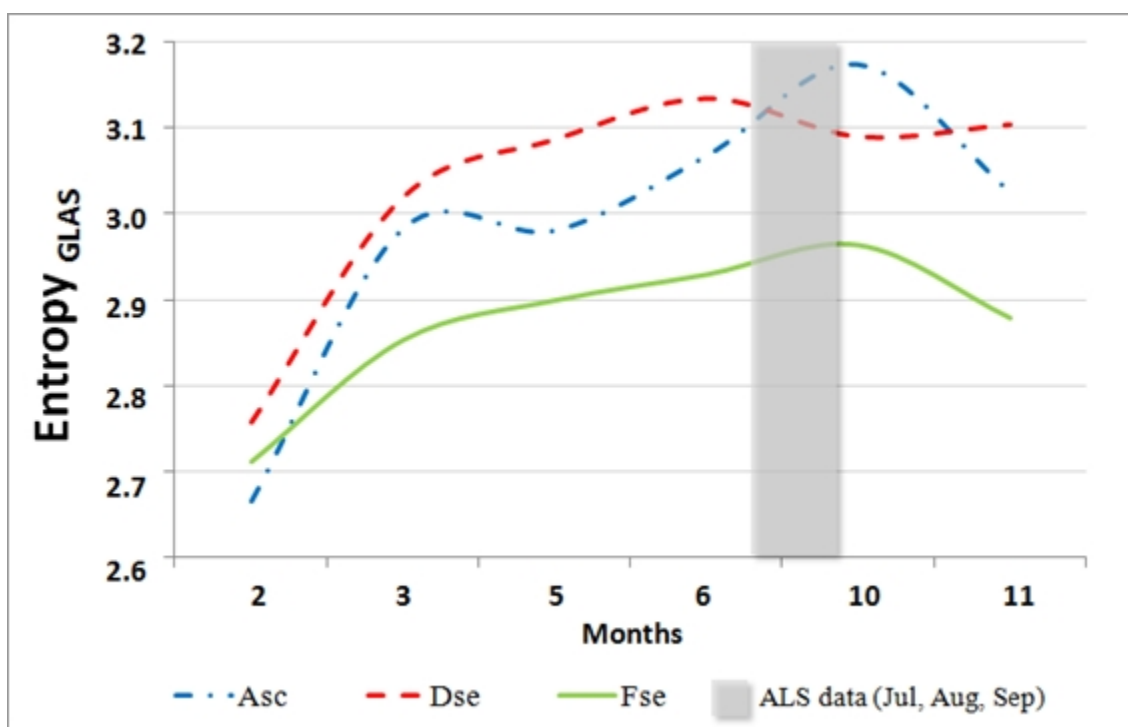
824 structural parameters than Anisotropy.

825

826

**Figure 1**

827

828

Dense Ombrophilous Forest (Dse)

Open Ombrophilous Forest with Lianas (Asc)

Semideciduous Forest Emergent Canopies (Fse)

829

830 **Figure 2**

831

832

833

834

835

836

837

838

839

840

841

842

843

844



845

**Figure 3**

847

848

849

850

851

852

853

854

855

856

857

858

859

860

861

862

863

864



865

**Figure 4**

867

868

869

870

871

872

873

874

875

876

877

878

879
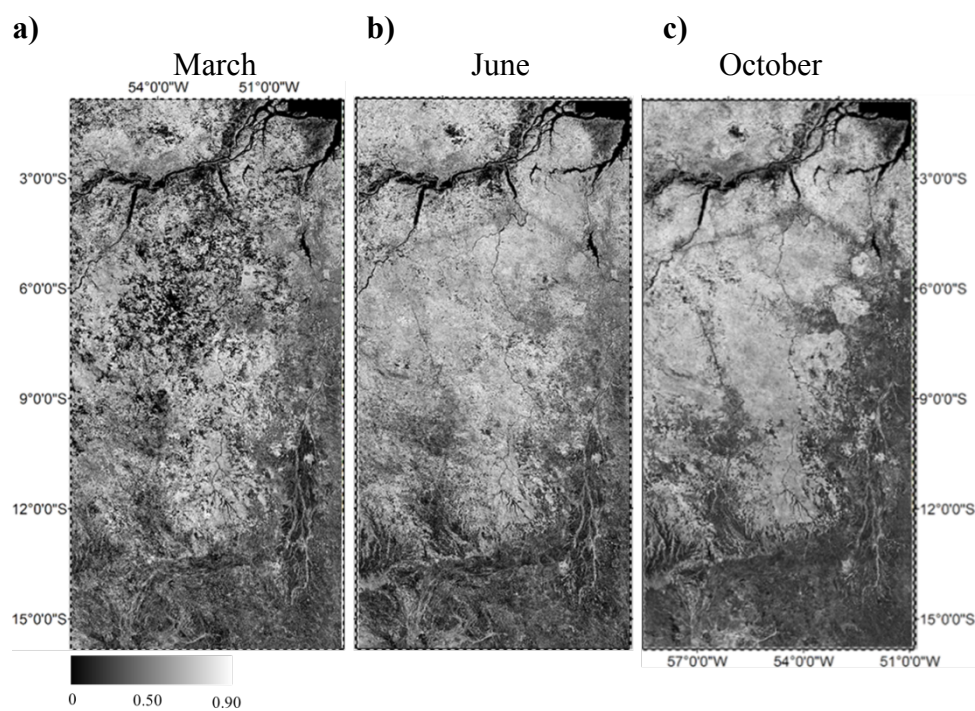


**Figure 5**

881

882

883

884

885

886

887

888

889

890

891

892

893

894



Plot with the following annotations inside: y=1.8657+2.1707x, $r^2=0.54$ (p<0.05), n=828, rmse=0.11. X-axis labeled Anisotropy$_{MOD}$ ranging from 0 to 0.8. Y-axis labeled Entropy$_{ALS}$ ranging from 1 to 4.

895

896    **Figure 6**

897

898

899

900

901

902

903

904

905

906

907

908

909



910

911 **Figure 7**

912

913

914

915

916

917

918



The figure shows a scatter plot with the following annotations:

$$y=-10.0885+7.4045x+-5.1854x^2$$
$$r^2=0.59$$
$$n=10000$$
$$rmse=0.11$$

Y-axis: SeaWinds$_{QSCAT}$ ($\sigma^0$), ranging from -11 to -6

X-axis: Anisotropy$_{MOD}$, ranging from 0 to 0.6

919

920    **Figure 8**

921

922

923

924

925

926

927

928

929

930

931

932

933

934



935

936    **Figure 9**

937

938

939

940

941

942

943

944

945

946

947

948    **APPENDIX A**

949



A
Entropy vs EVI
y=-0.8804+0.0158x
$r^2$=0.01 (p<0.05)

B
QSCAT ($\sigma^0$) vs EVI
$r^2$ = 0.31
y = -12.7281 + 11.2830x + -4.4197$x^2$

C
Entropy vs EVI
y=1.9054+1.9637x
$r^2$=0.24 (p<0.05)

950

951    **Figure A1**

952

953